Monthly Notices of the ROYAL ASTRONOMICAL SOCIETY

MNRAS **525,** 4121–4128 (2023) https://doi.org/10.1093/mnras/stad2579
Advance Access publication 2023 August 25

Multimessenger parameter inference of gravitational-wave and electromagnetic observations of white dwarf binaries

Peyton T. Johnson [1]★ Michael W. Coughlin [1]★ Ashlie Hamilton,[1] María José Bustamante-Rosell,[2] Gregory Ashton [3] Samuel Corey,[1] Thomas Kupfer,[4] Tyson B. Littenberg,[5] Draco Reed[1] and Aaron Zimmerman[2]

[1]*School of Physics and Astronomy, University of Minnesota, Minneapolis, MN 55455, USA*
[2]*Center for Gravitational Physics, University of Texas at Austin, 2515 Speedway, C1600, Austin, TX 78712, USA*
[3]*Department of Physics, Royal Holloway, University of London, TW20 0EX, UK*
[4]*Department of Physics and Astronomy, Texas Tech University, PO Box 41051, Lubbock, TX 79409, USA*
[5]*NASA Marshall Space Flight Center, Huntsville, AL 35811, USA*

Accepted 2023 May 2. Received 2023 May 2; in original form 2021 December 1

ABSTRACT

The upcoming *Laser Interferometer Space Antenna* (*LISA*) will detect a large gravitational-wave foreground of Galactic white dwarf binaries. These sources are exceptional for their probable detection at electromagnetic wavelengths, some long before *LISA* flies. Studies in both gravitational and electromagnetic waves will yield strong constraints on system parameters not achievable through measurements of one messenger alone. In this work, we present a Bayesian inference pipeline and simulation suite in which we study potential constraints on binaries in a variety of configurations. We show how using *LISA* detections and parameter estimation can significantly improve constraints on system parameters when used as a prior for the electromagnetic analyses. We also provide rules of thumb for how current measurements will benefit from *LISA* measurements in the future.

Key words: binaries: eclipsing – white dwarfs.

1 INTRODUCTION

The upcoming *Laser Interferometer Space Antenna* (*LISA*) will revolutionize gravitational-wave astronomy (Amaro-Seoane et al. 2017), opening a completely new frequency band beyond what has been studied so far using ground-based gravitational-wave interferometers such as Advanced LIGO (Aasi et al. 2015) and Advanced Virgo (Acernese et al. 2014), and pulsar timing arrays such as NANOGrav (Arzoumanian et al. 2020) and the Parkes Pulsar timing array (Goncharov et al. 2021). Planned for a nominal mission of 4 yr and an extended mission 6 yr further, *LISA* will detect not only extreme mass ratio inspirals or supermassive black hole mergers at low masses (Ruiter et al. 2010; Marsh 2011; Nissanke et al. 2012; Sesana 2021), but also compact objects covering ∼0.1 Hz to 10 mHz, the dominant source class of which is double white dwarf binaries, which have two stellar-mass compact objects with orbital periods less than 1 h. Their relatively short orbital periods slowly undergo orbital decay due to the emission of gravitational waves. This is in addition to binaries that contain other compact objects such as hot sub-dwarf stars, neutron stars, and possibly black holes. Short period binaries whose parameters we can measure in advance are known as 'verification' sources (Kupfer et al. 2018), as their gravitational-wave strain can be predicted based on parameters constrained by electromagnetic observations.

Time-domain optical surveys such as the Asteroid Terrestrial−impact Last Alert System (Tonry et al. 2018) and the Zwicky Transient Facility (ZTF; Bellm et al. 2018; Masci et al. 2018; Graham et al. 2019), among others, are detecting white dwarf binaries regularly, with more than a dozen sources already known (Burdge et al. 2019a, b; Coughlin et al. 2020; Burdge et al. 2020b). There are three types of systems that these surveys detect: eclipsing detached systems, ellipsoidal detached systems, and accreting systems (e.g. AM CVn systems, where a white dwarf accretes hydrogen-poor matter from a compact companion star). After their detection by the survey, these systems are followed-up with high cadence photometry by using instruments such as the Kitt Peak EMCCD Demonstrator (Coughlin et al. 2019) and CHIMERA (Harding et al. 2016) to measure their orbital decay through measurement of changes in the orbital phase of the binary. These measurements, typically focusing either on the 'eclipse' times for eclipsing systems or fits to the sinusoidal modulation phase, are then used to construct observed-minus-computed diagrams where the deviation in phase is measured relative to an object without orbital changes.

As white dwarf binaries will form a gravitational-wave foreground, understanding their contribution to the *LISA* spectrum will be important so they can be removed, studying the fainter and rarer signals underneath (Littenberg et al. 2020b). Population synthesis results point to more than ∼10 000 binaries expected to be individually resolvable, with all binaries with periods shorter than 15 min expected to be detected, no matter its location in our Galaxy (Lamberts et al. 2019). Studying the population of white dwarf binaries is

★ E-mail: joh15016@umn.edu (PTJ); cough052@umn.edu (MWC)

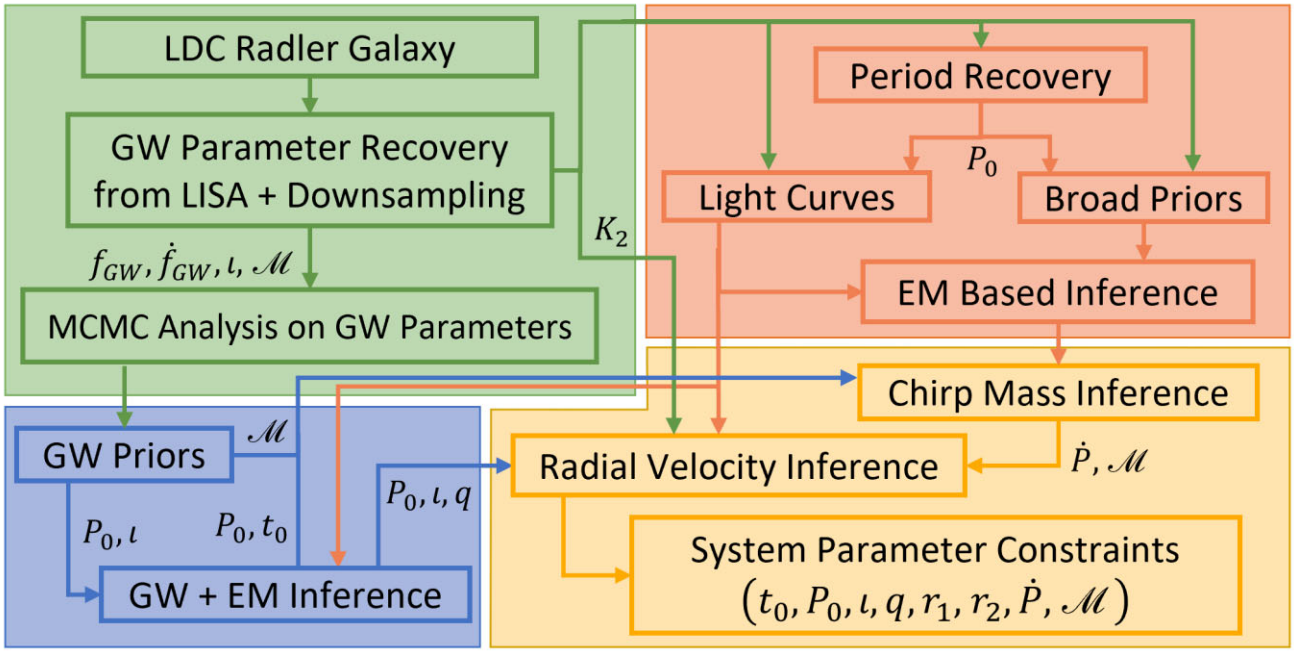

Figure 1. Flow chart of the data analysis pipeline. The pipeline starts with the LDC Radler Galaxy and each of the other steps in the top left panel involves only the gravitational-wave portion of the analysis. In the top-right and centre-left panels are steps pertaining to purely electromagnetic analysis and to joint gravitational-wave and electromagnetic analysis, respectively. The bottom panel displays the Bayesian inferences that are applied to the results of both the purely electromagnetic and joint analysis.

also interesting astrophysically. As inherently quantum objects, they probe quantum mechanics in a regime difficult to replicate on Earth due to the very high temperatures and densities involved (see e.g. Chandra et al. 2020). They are also likely to be the progenitors of Type Ia supernovae (Shen 2015), although the exact channel remains uncertain. In addition, they probe white dwarf structure (Fuller & Lai 2011), galactic structure (Breivik, Mingarelli & Larson 2019), binary stellar evolution (Nelemans & Tout 2005; Antonini, Toonen & Hamers 2017; Banerjee 2017; Kremer et al. 2018), accretion physics (Cannizzo & Nelemans 2015), and general relativity (Kupfer et al. 2019; Burdge et al. 2019a).

In general, *LISA* will make it possible to identify many white dwarf binaries that were bright enough to be picked up by optical surveys, but only through measurements of sky location, period, distance, and frequency will they be able to be identified as such in the surveys. Many previous works have pointed out that electromagnetic and gravitational-wave measurements will provide complementary views of the white dwarf binary population (see e.g. Nelemans, Yungelson & Zwart 2001, 2004; Shah, van der Sluys & Nelemans 2012; Shah & Nelemans 2014). For example, Shah & Nelemans (2014) have used Fisher-matrix based analyses to show improvements on parameter uncertainties accessible to both detectors, including distance to the source and masses of the objects. However, most previous analyses using Fisher matrices are limited by the technique, as they only hold in the limit of strong signals with Gaussian noise, and may underestimate the parameter uncertainties.

In this work, we will expand upon these previous methods by including a Bayesian inference based analysis based on state of the art data analysis pipelines built for *LISA*. In Section 2, we describe the simulation and Bayesian inference pipeline used for this study. In Section 3, we discuss the results of the analysis and implications for future observations with *LISA*. Section 4 summarizes our conclusions and forward outlook.

2 SIMULATION AND DATA ANALYSIS PIPELINE

Our work centres around a data analysis pipeline as illustrated in Fig. 1.

2.1 Gravitational-wave analysis

For our analysis, we used the `gbfisher` module from LDASOFT (Littenberg et al. 2020a) to simulate ∼20 000 white dwarf binary systems, each with all of the parameters described below. Due to computational limitations, we narrowed down our multimessenger analysis to a subsample consisting of ∼200 binaries. For demonstration purposes, we constructed two sets of binaries, an eclipsing set and a non-eclipsing set. White dwarf binaries with inclinations between 0° and 80° were placed in the non-eclipsing set while binaries with inclinations between 80° and 90° were placed in the eclipsing set. Both sets were reduced further by removing all binaries with periods less than 4 min or greater than 20 min as well as binaries with an SNR of less than 20 or greater than 150. A subset of 100 binaries was randomly sampled from each of the eclipsing and non-eclipsing binary sets. We note that these sets are not meant to be representative of the true population; future analyses will focus on such representative sets.

We used the `gbmcmc` module from LDASOFT (Littenberg et al. 2020a) to provide the gravitational-wave parameter estimates for our simulated set of white dwarf binaries. The `gbmcmc` module used a reversible-jump Markov Chain Monte Carlo (MCMC) method to identify the range of plausible models for each binary in the down-sampled set. Next, `gbmcmc` produced posterior distributions for the recovered parameters which included the initial gravitational-wave frequency, f_{GW}, the time derivative of frequency, $\dot{f}_{GW}$, the gravitational-wave amplitude, A, the inclination, ι, the polarization

angle, the initial gravitational-wave phase, and the ecliptic colatitude and longitude. From these quantities, we could derive the chirp mass, $\mathcal{M}$, which is related to the parameters $f_{\rm GW}$ and $\dot{f}_{GW}$ by

$$\mathcal{M} = \frac{c^3}{G}\left(\frac{5}{96}\pi^{-\frac{8}{3}} f_{\rm GW}^{-\frac{11}{3}} \dot{f}_{\rm GW}\right)^{\frac{3}{5}}. \quad (1)$$

In addition, we also used these quantities to derive the time rate of change of period given by

$$\dot{P}_0 = \frac{2\dot{f}_{\rm GW}}{f_{\rm GW}^2} = \left(\frac{\dot{f}_{\rm GW}}{f_{\rm GW}}\right) P_0, \quad (2)$$

which is useful for comparison with the $\dot{P}_0$ and $\mathcal{M}$ parameters recovered by optical surveys.

2.2 Light curve analysis

We produced simulated light curves for the white dwarf binaries using the PYTHON package ELLC (Maxted 2016). The light curve generation depended primarily on the initial period P_0, the mid-eclipse time of the primary eclipse, t_0, the inclination, ι, the mass ratio, q, and the ratios of the radii of the primary and secondary objects to the semimajor axis, r_1 and r_2, respectively. Additional parameters in the light curve model were the surface brightness ratio J, the limb darkening coefficients ldc_1 and ldc_2, the gravity darkening coefficients, gdc_1 and gdc_2, and coefficients for the simplified reflection model, heat_1 and heat_2.

For our light curve analysis, we simulated two sets of observations. The first was a long-baseline cadence simulated over roughly 8 yr with an average observational cadence of 3 d and noise consistent with expected ZTF g-band measurements. This simulated the type of photometric data expected for using optical surveys such as the ZTF or the Vera Rubin Observatory for identification of white dwarf binaries. Our simulated long baseline data was most useful for identifying the object's period, P_0. We note that here we corrected for the orbital period evolution using a Post-Newtonian approximation to find that the period evolves according to

$$P = P_0\left(1 - \frac{t}{\tau}\right)^{\frac{3}{8}}, \quad (3)$$

where τ is an approximation of the gravitational-wave inspiral time-scale given by

$$\tau = -\frac{3}{8}\frac{P_0}{\dot{P}}.$$

The second type of simulated observation was of high-cadence follow-up data such as provided by KPED (Coughlin et al. 2019) and CHIMERA (Harding et al. 2016). For each binary, we constructed 25 sets of simulated observations taken over one night of observations, on average captured at intervals of 120 ± 5 d.

Amongst other parameters, these observations captured the mid-eclipse times t_i, for each set of nightly data. These t_i estimates were useful for estimating $\dot{P}_0$ and therefore $\dot{f}_{GW}$; the estimates were related to the mid-eclipse time observations by

$$\Delta t_{\rm eclipse}\,(t_i - t_0) = \left(\frac{1}{2}\dot{f}_{\rm GW}(t_0)\,(t_i - t_0)^2 + \frac{1}{6}\ddot{f}_{\rm GW}(t_0)\,(t_i - t_0)^3 + \ldots\right) P\,(t_0). \quad (4)$$

where $P(t_0)$ is the orbital period at the reference epoch, $f_{\rm GW}(t_0)$, $\dot{f}_{\rm GW}(t_0)$, etc, are the orbital frequency and its time derivatives at the reference epoch, and $t_i - t_0$ is the time elapsed since the reference epoch. We note that both the simulated survey and high cadence observations accounted for the change in period.

The high-cadence photometry also provided constraints on the orbital inclination. While the gravitational-wave recoveries were sensitive to binary orientation such that they ranged from 0 to 180°, the light curves we simulated were not capable of distinguishing between a system facing towards and a system facing away from an observer. For this reason, when using our gravitational-wave observations as priors for the electromagnetic analysis, we mapped the gravitational-wave inclination posteriors onto the interval 0° through 90° using the rescaling $\iota' = 90° - |\,\iota - 90°\,|$ where ι' is the gravitational-wave inclination, ι, mapped onto the 0 to 90° interval.

The light curves were sensitive to a number of parameters that the gravitational-wave observations were not. For example, in systems undergoing strong ellipsoidal deformation, the light curve observations loosely constrained the binary's mass ratio, $q = \frac{m_2}{m_1}$. For this reason, we drew q randomly for each binary from a uniform distribution extending from 0.25 to 1. Occasionally, this method yielded a mass ratio which caused the primary mass to exceed the Chandrasekhar limit; in these cases, we increased the lower bound for the mass ratio such that the Chandrasekhar limit couldn't be exceeded.

The light curves were also sensitive to the scaled radii r_1 and r_2 of the system. To derive these values, we used the system's chirp mass and simulated mass ratio to calculate the individual masses, m_1 and m_2, using the expressions

$$m_1 = (1+q)^{\frac{1}{5}}\, q^{-\frac{3}{5}}\,\mathcal{M} \quad (5)$$

$$m_2 = (1+q)^{\frac{1}{5}}\, q^{\frac{2}{5}}\,\mathcal{M} \quad (6)$$

We obtained estimates for the radii of each white dwarf, R_1 and R_2, by fitting a univariate spline curve to a set of white dwarf masses and their corresponding radii and then evaluating the spline for masses m_1 and m_2, respectively. We obtained a rough approximation of the semi-major axis a by using the fact that the GW frequency is twice the orbital frequency and solving Kepler's Third law to get the expression:

$$a = \left[\frac{G\,(m1 + m2)}{(\pi\, f_{\rm GW})^2}\right]^{\frac{1}{3}}. \quad (7)$$

We then scaled the white dwarf radii in terms of the semimajor axis to acquire the dimensionless scaled radii values given by $r_1 = \frac{R_1}{a}$ and $r_2 = \frac{R_2}{a}$.

The light curves produced by ELLC provided an estimate for flux as a function of time. To provide realistic error bars for the analyses, we took CHIMERA data collected for the 6.9 min binary (Burdge et al. 2019a) from July 2018 and superimposed those error bars upon the simulated light curve. When performing the inference, we also included an arbitrary scaling parameter to account for any offsets in the flux due to the way the photometry is compared to the neighbour stars.

2.3 Combined gravitational-wave and electromagnetic analysis

We employed the PYTHON package BILBY (Ashton et al. 2019) to perform Bayesian inferences on the simulated white dwarf binary light curves. We analysed the light curves using two sets of priors; the first was a broad set of priors designed to be uninformative and the second used the gravitational-wave posteriors obtained from `gbmcmc` as priors for the electromagnetic analysis. The former case

simulated the situation we are currently in, where the gravitational-wave data is unavailable or the white dwarf binary is not detected in gravitational-waves, while the latter simulated the utilization of both gravitational-wave and electromagnetic data to improve binary system parameter estimates.

In the case of the broad priors, we used a distribution which was uniform in cosine of inclination from 0 to 1 as our inclination prior. We used the PYTHON package PERIODFIND (Coughlin et al. 2021), a GPU-based implementation of the analysis of variance (Schwarzenberg-Czerny 1998) algorithm, to estimate the period, P_0, and its uncertainty, σ_{P_0} for a particular object. Using these results, we then constructed a broad Gaussian period prior with a mean of P_0 and a standard deviation of σ_{P_0}. In the case of the gravitational-wave based priors, we performed a Gaussian kernel density estimate of both the inclination and period posteriors from `gbmcmc` and we used these to construct the parameter distributions which served as our inclination and period priors. In both analyses, each of the remaining parameters, mid-eclipse time, mass ratio, radii, and the scale factor were given uniform priors. The uniform prior for the mid-eclipse time extended from $t_0 - \frac{P_0}{2}$ to $t_0 + \frac{P_0}{2}$, for the mass ratio the prior extended from 0.15 to 1, and for both the scaled radii and the scale parameter, the priors extended from 0 to 1.

In order to widen the overall parameter space and keep our sampling as unbiased as possible, the remaining parameters were randomly generated due to the difficulties in constructing model-based surface brightness ratios, limb-darkening and gravity-darkening coefficients, and reflection coefficients for the light curves. For each individual binary, the surface brightness ratio, the limb-darkening coefficients, and the gravity-darkening coefficients were randomly generated from the range between 0 and 1 and for the light curve analyses, uniform priors extending from 0 to 1 were used for each of these parameters. Similarly, the reflection model coefficients were randomly generated from the range between 0 and 5 with uniform priors from 0 to 5 used for the light curve analyses.

A Gaussian likelihood function was used, appropriate for the error bars associated with optical data, computed by comparing the flux and flux uncertainties to the simulated light curve model. We varied the parameters P_0, t_0, ι, q, r_1, r_2, J, ldc_1, ldc_2, gdc_1, gdc_2, heat_1, heat_2, and the scale factor during the inference. To carry out the Bayesian inferences we used the PYTHON package BILBY, which uses the PYTHON package PYMULTINEST (Buchner et al. 2014). In turn, PYMULTINEST used the C-library `MultiNest` (Feroz, Hobson & Bridges 2009) as its backend, a tool shown to be useful for high-dimensional sampling problems in many areas of astrophysics.

2.4 Combining multinight observations

Using the expression for chirp mass given by equation (1) and $\Delta t_{\mathrm{eclipse}}$ given by equation (4), we used the residual eclipse times derived from each observation to fit for the chirp mass and initial period of each white dwarf binary system. To do so, we constructed a Gaussian likelihood using the median and standard deviation of the eclipse time residuals calculated from each observation. For our initial period priors, we constructed Gaussian kernel density estimates of the period posteriors obtained from the light curve fitting process. For the electromagnetic analyses we used a uniform prior for chirp mass extending from 0.05 to 1.25 solar masses, for the combined analyses we constructed a Gaussian kernel density estimate of the chirp mass distributions constructed using the f_{GW} and $\dot{f}_{\mathrm{GW}}$ posteriors obtained from `gbmcmc`.

2.5 Radial velocities

The final set of simulated observations were radial velocity measurements of the white dwarf binaries. In general, these are required to make accurate estimates of the individual masses of the system. The radial velocity of the secondary object, K_2, was related to the orbital period, chirp mass, mass ratio, and inclination by

$$K_2 = \left(\frac{2\pi G\mathcal{M}}{P_0}\right)^{\frac{1}{3}} \frac{\sin\iota}{q^{\frac{1}{5}}(1+q)^{\frac{3}{5}}}. \tag{8}$$

Passing the system's chirp mass, the simulated mass ratio, the inclination recovered by `gbfisher`, and the period recovered by `gbfisher` into equation (8) gave us the radial velocity of the secondary white dwarf. We constructed a Gaussian likelihood using the period recovered by `periodfind` as our input data and a fixed estimate of uncertainty on the radial velocity of $\pm 50\,\mathrm{km\,s^{-1}}$. We constructed Gaussian kernel density estimates of the inclination and mass ratio posterior obtained from the light curve fitting process. Additionally, we constructed a Gaussian kernel density estimate of the chirp mass posterior obtained from fitting the residual eclipse times. Then we used the kernel density estimates to produce chirp mass, inclination, and mass ratio priors which were used along with the likelihood to carry out a Bayesian inference.

3 RESULTS

For analysis and interpretation purposes, the white dwarf binary systems can largely be categorized as either eclipsing or non-eclipsing systems. Therefore, in the following, we will generally separate out our conclusions for each object type for the different parameters.

Period constraints. The period constraints are typically several orders of magnitude more precise for the broad and combined posteriors than for the gravitational-wave priors, an effect clearly illustrated in the upper corner plots in Figs 2 and 3 as well as in Table 1 and Table 2. The uncertainty on the period recovered for the broad and combined posteriors shows that over an 8 yr period we can generally expect to accumulate a total error less than the orbital period; in line with the expectation that orbital cycle count is well established.

Inclination constraints. Eclipsing binary light curves, such as the ones magnified on the right in Fig. 2, have strongly constrained inclination, as properties of the light curve such as eclipse duration and eclipse depth are closely related to inclination. The resolvability of the eclipses, especially shallower ones, depends heavily on the noise level of the light curve. In this sense, a system that is 'eclipsing' depends not only on its angle relative to the detector, but also the detector sensitivity itself. For a handful of the 'eclipsing' binaries in our simulated set, the recovered parameters are at a precision more akin to the non-eclipsing binaries due to the fact that the eclipses were buried within the noise. Unsurprisingly, Fig. 4 shows that the inclinations of the eclipsing binaries, especially those recovered solely through electromagnetic analyses, are better constrained than for the non-eclipsing binaries. For eclipsing systems with inclinations above $\sim 75^\circ$, the inclinations recovered purely from gravitational-wave data and purely from electromagnetic data are both constrained to a precision of within $\sim 2^\circ$ of the true inclinations.

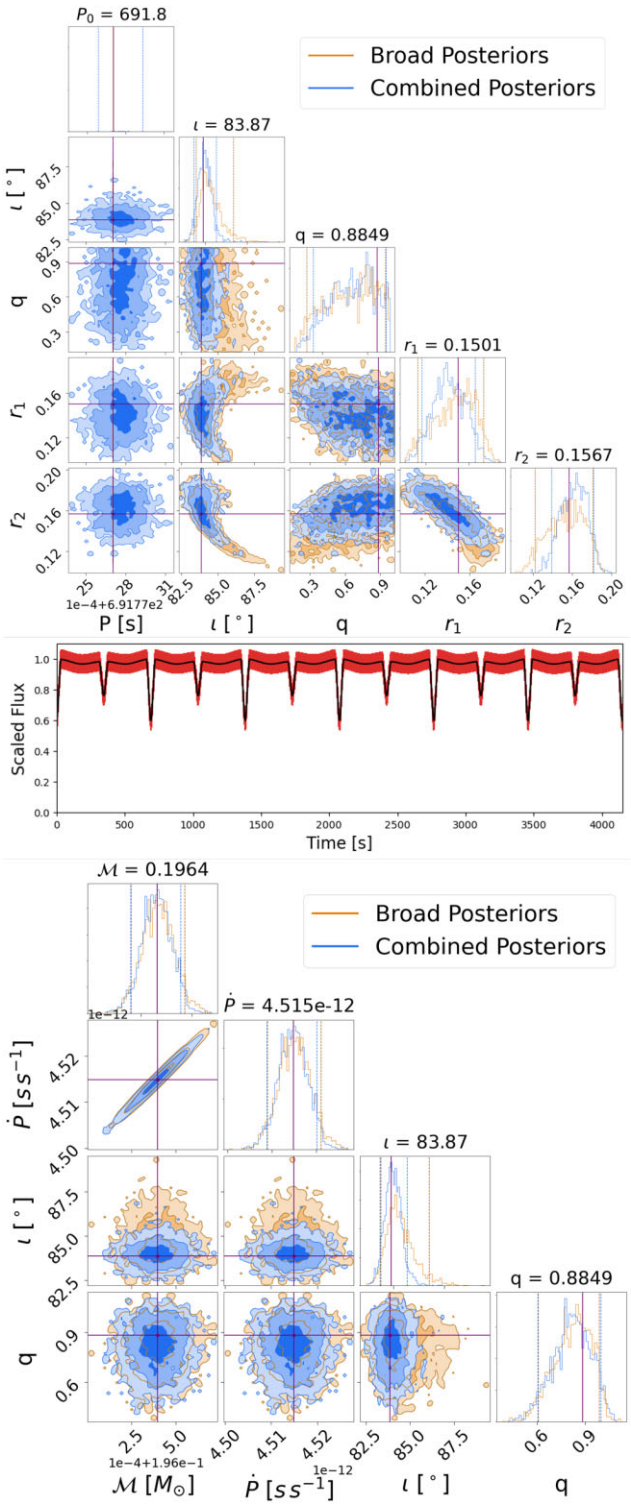

Figure 2. Corner plots and light curve for an example eclipsing white dwarf binary. Top: Corner plot comparing the posteriors obtained from the light curve inference using the two prior sets. Centre: Light curve plot displaying the normalized luminosity as a function of time over several orbits. Bottom: Corner plot comparing the posteriors obtained from the radial velocity inference using the two prior sets.

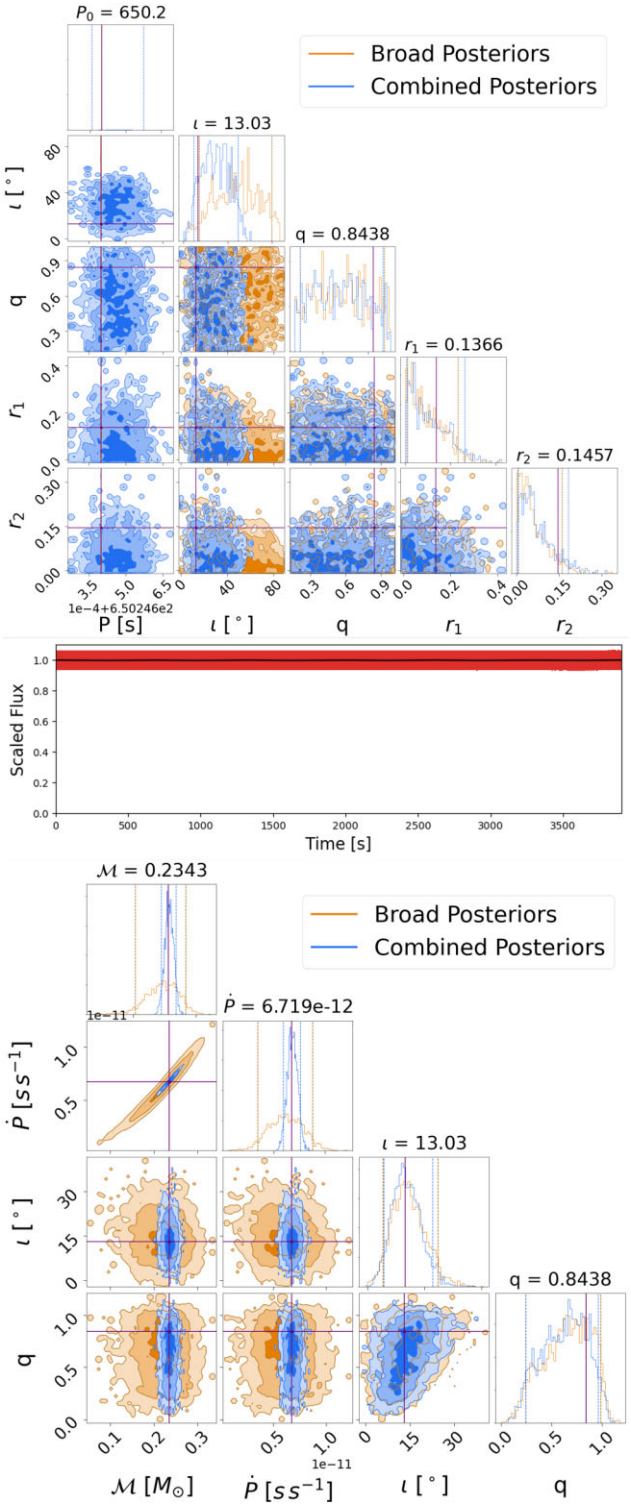

Figure 3. Corner plots and light curve for an example non-eclipsing white dwarf binary. Top: Corner plot comparing the posteriors obtained from the light curve inference using the two prior sets. Centre: Light curve plot displaying the normalized luminosity as a function of time over several orbits. Bottom: Corner plot comparing the posteriors obtained from the radial velocity inference using the two prior sets.

Table 1. Table of recovered parameters for the example eclipsing white dwarf binary shown in Fig. 2 for each prior set.

	Gravitational-wave	Electromagnetic	Combined
ι (°)	$82.34^{+2.63}_{-2.89}$	$84.29^{+1.81}_{-1.02}$	$83.96^{+0.86}_{-0.75}$
P_0 (s)	$691.77277^{+0.00017}_{-0.00017}$	$691.77270510^{+0.00000064}_{-0.00000062}$	$691.77277^{+0.00017}_{-0.00018}$
$\dot{P}$(s s^{-1})	$0.51^{+0.14}_{-0.14} \times 10^{-11}$	$0.45151^{+0.00060}_{-0.00061} \times 10^{-11}$	$0.45148^{+0.00054}_{-0.00059} \times 10^{-11}$
$\mathcal{M}$ (M$_\odot$)	$0.211^{+0.032}_{-0.036}$	$0.19640^{+0.00016}_{-0.00016}$	$0.19639^{+0.00014}_{-0.00015}$
q		$0.83^{+0.16}_{-0.22}$	$0.82^{+0.18}_{-0.22}$
R_1 ($R_\odot$)		$1.91^{+0.33}_{-0.46} \times 10^{-2}$	$1.83^{+0.32}_{-0.33} \times 10^{-2}$
R_2 ($R_\odot$)		$1.99^{+0.35}_{-0.41} \times 10^{-2}$	$2.09^{+0.26}_{-0.30} \times 10^{-2}$

Table 2. Table of recovered parameters for the example non-eclipsing white dwarf binary shown in Fig. 3 for each prior set.

	Gravitational-wave	Electromagnetic	Combined
ι (°)	$33.9^{+17.1}_{-23.2}$	$13.9^{+10.7}_{-8.6}$	$13.2^{+9.7}_{-7.6}$
P_0 (s)	$650.24647^{+0.00011}_{-0.00011}$	$650.24639894^{+0.00000052}_{-0.00000055}$	$650.24646^{+0.00011}_{-0.00011}$
$\dot{P}$(s s^{-1})	$0.687^{+0.086}_{-0.085} \times 10^{-11}$	$0.62^{+0.26}_{-0.28} \times 10^{-11}$	$0.680^{+0.082}_{-0.084} \times 10^{-11}$
$\mathcal{M}$ (M$_\odot$)	$0.237^{+0.018}_{-0.018}$	$0.222^{+0.053}_{-0.066}$	$0.236^{+0.017}_{-0.018}$
q		$0.67^{+0.32}_{-0.42}$	$0.65^{+0.32}_{-0.40}$
R_1 ($R_\odot$)		$1.07^{+1.99}_{-0.99} \times 10^{-2}$	$1.19^{+2.28}_{-1.06} \times 10^{-2}$
R_2 ($R_\odot$)		$0.60^{+1.54}_{-0.53} \times 10^{-2}$	$0.77^{+1.65}_{-0.66} \times 10^{-2}$

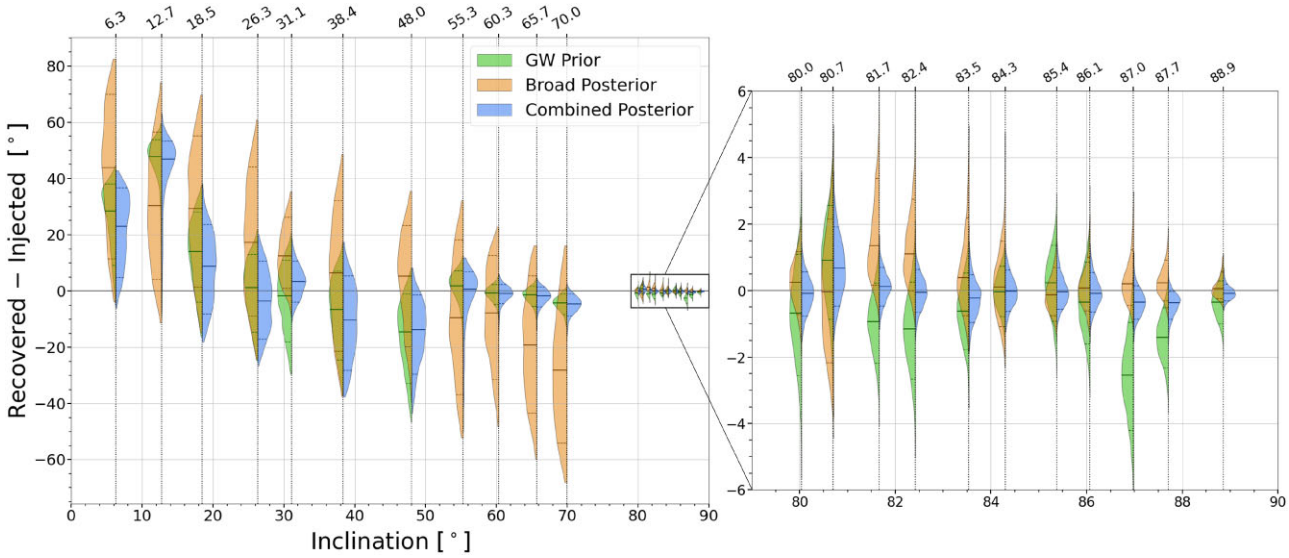

Figure 4. Recovered − injected diagram with the residual inclination distributions from the light curve inference plotted against the system inclinations for a sample of eclipsing and non-eclipsing binaries. Each 'violin' corresponds to a white dwarf binary system and displays two inclination posteriors corresponding to the two sets of priors as well as the corresponding gravitational-wave inclination prior. The horizontal lines embedded in each distribution mark the 10th, 50th, and 90th percentiles of the distribution.

For non-eclipsing systems the level of precision on the inclination recovered through gravitational-wave analysis increases with increasing inclination of the systems. For example, the lower inclination binaries in Fig. 4 with inclinations below ∼45° display levels of precision on the order of ∼10° whereas non-eclipsing systems with higher inclinations constrain the system inclinations to within a few degrees. In contrast, the constraints on the inclinations recovered from purely electromagnetic analyses of non-eclipsing binaries show little to no correlation with the inclinations of the systems, with precision on the order of ∼40° regardless of inclination.

Chirp mass constraints. As described above, the potential measurements of $\dot{P}$ yield measurements of chirp mass. Shorter periods tend to lead to better recovery of $\dot{P}$ which in turn leads to more precise measurements of the chirp mass. The trend is displayed prominently in Fig. 5 where we show the recovered chirp mass distributions plotted against period; we also see that for eclipsing binaries and short period non-eclipsing binaries, inclusion of optical

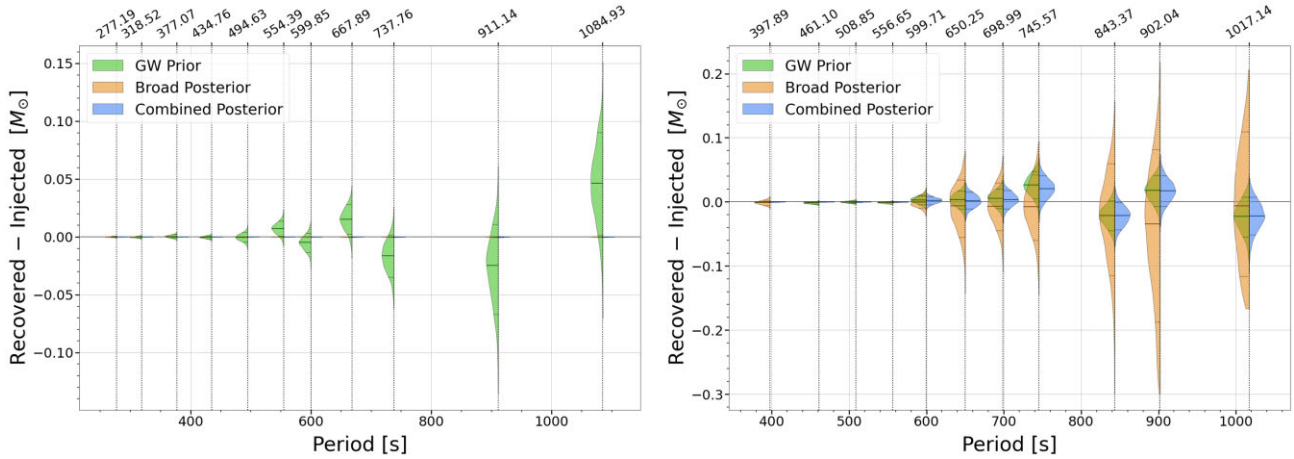

Figure 5. Recovered − injected diagrams with the residual chirp mass distributions plotted against the system orbital periods for a sample of eclipsing (left) and non-eclipsing binaries (right). Each 'violin' corresponds to a white dwarf binary system and displays two chirp mass posteriors corresponding to the two sets of priors as well as the corresponding calculated gravitational-wave chirp mass prior. The horizontal lines embedded in each distribution mark the 10th, 50th, and 90th percentiles of the distribution.

data reaches and surpasses the level of precision in the chirp mass estimate obtained from the gravitational-wave information alone. In particular, we found that for non-eclipsing binaries with periods below ∼11 min, the measurement of chirp mass obtained from the high-cadence optical follow-up by itself yielded a level of precision comparable to the measurements obtained from *LISA* analysis alone; an effect which presents itself in the chirp mass of the non-eclipsing binary shown in Fig. 5 as well as in Table 2. In contrast, non-eclipsing binaries with longer orbital periods showed chirp mass recovery precision more akin to the level of precision obtained from gravitational-wave analyses. It is in this regime, where the precision in chirp mass recovery obtained from gravitational-wave and electromagnetic analyses is similar, that the combined analysis proves the most benefit and shows the greatest improvement in chirp mass recovery over the measurements obtained by using each source individually.

Mass ratio constraints. Using purely gravitational-wave based observations, it is not possible to constrain the mass ratio q. Additionally, due to the difficulty of a priori knowing the gravity-darkening and limb-darkening coefficients, ellipsoidal variations in the light curve offer, at most, a model-dependent constraint on the mass ratio q. More promising, however, is the use of mass–radius relations in eclipsing systems with detectable $\dot{P}$, such as for ZTF J2243+5242 (Burdge et al. 2020a). Inclusion of a radial velocity, allows for small improvements in the mass ratio recovery and thus the uncertainty in the radial velocity dictates to some effect how well the mass ratio is constrained. As expected from equation (8), the constraint on the mass ratio improves when the inclination, chirp mass, and period are well constrained. This is the case for most eclipsing binaries, whereas for non-eclipsing binaries, the limited improvements in mass ratio recovery due to the radial velocity constraint are less pronounced.

4 CONCLUSION

We constructed a robust data analysis pipeline designed for use with *LISA* for carrying out joint analyses of gravitational-wave and electromagnetic information from white dwarf binary systems. Using the results of our pipeline, we observed a number of improvements in parameter space estimation offered by using Bayesian inference to carry out a combined analysis. In particular, we saw that combined analyses led to increases in precision in period, inclination, and chirp mass, and quantified these improvements across the parameter space. Additionally, we observed that minor improvements in the constraints on the mass ratio could be made by incorporating radial velocity into the parameter inference, where we took a basic model of radial velocity measurements from potential time-resolved spectroscopy.

While our framework is a strong step forward relative to the current paradigm of using Fisher matrices to make parameter estimates, the pipeline for combining gravitational-wave and electromagnetic analyses is currently limited by the computational power available for running large scale simulations of white dwarf binary populations, as well as the subsequent parameter recovery processes. In the future, we aim to adapt our framework to enable population level studies to bring us closer to the goal of being capable of simulating realistic gravitational-wave data for existing binary systems to make as accurate projections for LISA as possible. Additionally, we will aim to incorporate more sophisticated simulations of spectroscopic data as well as simulated distance estimates such as those provided by Gaia (Brown et al. 2021) into the parameter recovery portion of our pipeline, with the goal of automating the process for the white dwarf binaries that experiments such as ZTF are finding (Burdge et al. 2020b).

Looking forward, we intend to build out the light curve analysis used on the simulated data and apply it to non-simulated electromagnetic data collected by systems such as KPED (Coughlin et al. 2019). Before *LISA* flies, these observations can be used to track the period evolution and eclipse timing of verification binaries identified now before gravitational-wave data is available. Measurements of this kind will prepare these systems for the first multimessenger analyses once *LISA* data becomes available. We are using KPED to observe short-period white dwarf binaries in a dedicated program regularly, e.g (Burdge et al. 2019a; Coughlin et al. 2020), and can use these observations to track their period evolution. The period evolution of these objects can be used to look for gravitational-wave emission, or other physical processes that change the period. We look forward to having characterized as many of these systems as possible in preparation for *LISA*.

ACKNOWLEDGEMENTS

PTJ and AH thank the Undergraduate Research Opportunities Program at the University of Minnesota for funding their work. MWC acknowledges support from the National Science Foundation with grant numbers PHY-2010970 and OAC-2117997. AZ and MJB-R acknowledge support from the National Science Foundation with grant number PHY-1912578. Portions of this work were performed during the CCA LISA Sprint, supported by the Simons Foundation. The authors acknowledge the Minnesota Supercomputing Institute[1] at the University of Minnesota for providing resources that contributed to the research results reported within this paper under project 'Identification of Variable Objects in the Zwicky Transient Facility'.

DATA AVAILABILITY STATEMENT

The software described in this article is available at https://github.com/mcoughlin/gwemlisa. The simulations produced for this article will be shared on reasonable request to the corresponding author.

REFERENCES

Aasi J. et al., 2015, Class. Quantum Gravity, 32, 074001
Acernese F. et al., 2014, Classical Quantum Gravity, 32, 024001
Amaro-Seoane P. et al., 2017, arXiv e-prints
Antonini F., Toonen S., Hamers A. S., 2017, ApJ, 841, 77
Arzoumanian Z. et al., 2020, ApJ, 905, L34
Ashton G. et al., 2019, ApJS, 241, 27
Banerjee S., 2017, MNRAS, 473, 909
Bellm E. C. et al., 2018, Publ. Astron. Soc. Pac., 131, 018002
Breivik K., Mingarelli C. M. F., Larson S. L., 2019, ApJ, 901, 9

[1]http://www.msi.umn.edu

Brown A. G. A. et al., 2021, A&A, 649, A1
Buchner J. et al., 2014, A&A, 564, A125
Burdge K. B. et al., 2019a, Nature, 571, 528
Burdge K. B. et al., 2019b, ApJ, 886, L12
Burdge K. B. et al., 2020a, ApJ, 905, 32
Burdge K. B. et al., 2020b, ApJ, 905, 32
Cannizzo J. K., Nelemans G., 2015, ApJ, 803, 19
Chandra V., Hwang H.-C., Zakamska N. L., Cheng S., 2020, ApJ, 899, 146
Coughlin M. W. et al., 2019, MNRAS, 485, 1412
Coughlin M. W. et al., 2020, MNRAS, 494, L91
Coughlin M. W. et al., 2021, MNRAS, 505, 2954
Feroz F., Hobson M. P., Bridges M., 2009, MNRAS, 398, 1601
Fuller J., Lai D., 2011, MNRAS, 412, 1331
Goncharov B. et al., 2021, ApJ, 917, L19
Graham M. J. et al., 2019, Publ. Astron. Soc. Pac., 131, 078001
Harding L. K. et al., 2016, MNRAS, 457, 3036
Kremer K., Chatterjee S., Breivik K., Rodriguez C. L., Larson S. L., Rasio F. A., 2018, Phys. Rev. Lett., 120, 191103
Kupfer T. et al., 2018, MNRAS, 480, 302
Kupfer T. et al., 2019, ApJ, 878, L35
Lamberts A., Blunt S., Littenberg T. B., Garrison-Kimmel S., Kupfer T., Sanderson R. E., 2019, MNRAS, 490, 5888
Littenberg T. B., Cornish N. J., Lackeos K., Robson T., 2020a, tlittenberg/ldasoft:GBMCMC v1.0.1
Littenberg T. B., Cornish N. J., Lackeos K., Robson T., 2020b, Phys. Rev. D, 101, 123021
Marsh T. R., 2011, Class. Quantum Gravity, 28, 094019
Masci F. J. et al., 2018, Publ. Astron. Soc. Pac., 131, 018003
Maxted P. F. L., 2016, A&A, 591, A111
Nelemans G., Tout C. A., 2005, MNRAS, 356, 753
Nelemans G., Yungelson L. R., Zwart S. F. P., 2001, A&A, 375, 890
Nelemans G., Yungelson L. R., Zwart S. F. P., 2004, MNRAS, 349, 181
Nissanke S., Vallisneri M., Nelemans G., Prince T. A., 2012, ApJ, 758, 131
Ruiter A. J., Belczynski K., Benacquista M., Larson S. L., Williams G., 2010, ApJ, 717, 1006
Schwarzenberg-Czerny A., 1998, Open Astron., 7, 43
Sesana A., 2021, Frontiers Astron. Space Sci., 8, 7
Shah S., Nelemans G., 2014, ApJ, 790, 161
Shah S., van der Sluys M., Nelemans G., 2012, A&A, 544, A153
Shen K. J., 2015, ApJ, 805, L6
Tonry J. L. et al., 2018, Publ. Astron. Soc. Pac., 130, 064505

This paper has been typeset from a TEX/LATEX file prepared by the author.